Green Energy and Fuel Research

Scilight

Article

Performance Evaluation of Boiling-Based Two-Phase Immersion Cooling for Lithium-Ion Battery Modules Using Different Coolants and Discharge Rates

Wei-Mon Yan [1], Wen-Kai Wang [1], Chun-Han Li [2,*], and Saman Rashidi [3,*]

[1] Department of Energy and Refrigerating Air-Conditioning Engineering, National Taipei University of Technology, Taipei 10608, Taiwan
[2] Department of Energy and Refrigerating Air-Conditioning Engineering, National Kaohsiung University of Science and Technology, Kaohsiung 824004, Taiwan
[3] Department of Energy, Faculty of New Sciences and Technologies, Semnan University, Semnan 35131-19111, Iran
* Correspondence: wxes605896321@nkust.edu.tw (C.-H.L.); samanrashidi3983@gmail.com (S.R.)
Received: 30 July 2026; Revised: 3 October 2026; Accepted: 20 October 2026; Published: 29 October 2026

Abstract: In this numerical study, a boiling-based two-phase immersion cooling system is designed for lithium-ion batteries. However, systematic cross-coolant comparisons linking boiling onset, vapor generation, and module temperature uniformity under a common hydrodynamic condition remain limited. To address this gap, the Volume of Fluid (VOF) method, together with the transient solution method and the Lee model, is used to simulate boiling, evaporation, and two-phase flow of coolants after heating in the lithium-ion battery cooling module. FS49, SF33, Novec 7000, and R141b are considered as the coolants. All coolant cases were evaluated at a fixed Reynolds number, Re = 500, defined using the liquid-phase inlet properties and the inlet diameter, to provide a common hydrodynamic basis for comparison. The module's temperature distribution, average temperature, maximum temperature difference, temperature standard deviation, and gas-phase volume fraction results are examined at different discharge rates. At 9C, the low-boiling R141b triggered nucleate boiling earlier, reducing the maximum temperature by 14.81 °C (25.4%) compared to single-phase FS49. The coolant boiling point is identified as a critical parameter; phase-change media reduced internal temperature differences by 10.77–14.8 °C relative to single-phase flow by effectively flattening temperature rise curves via latent heat. R141b, with a gas-phase generation of approximately 0.7, has the highest gas-phase volume fraction among the four coolants, exhibiting superior heat-dissipation capabilities, with an average temperature of only 37.3 °C, a 27.1% reduction compared to FS49. The design of a two-phase immersion cooling system must balance the benefits of latent heat of vaporization against the adverse effects of bubble accumulation on the flow field. Ultimately, this work quantifies the roles of latent heat and convection, offering a vital numerical reference for optimizing high-power battery cooling media and flow configurations.

Keywords: lithium-ion battery; boiling-based immersion cooling; latent heat; temperature distribution; lee model

1. Introduction

Lithium-ion batteries (LIBs) are widely used in electric vehicles, residential energy storage, and grid-scale energy storage systems because of their high energy density, long cycle life, and stable power output. Lithium iron phosphate (LFP) batteries, in particular, have received increasing attention in energy-storage applications because of their favorable thermal stability, safety, and service life. Nevertheless, heat generated during high-rate charging and discharging can lead to elevated cell temperatures and non-uniform temperature distributions within battery modules, thereby accelerating battery degradation and increasing thermal safety risks [1–8]. Effective battery thermal management systems (BTMSs) are therefore essential for maintaining battery performance, durability, and operational safety. Conventional BTMS strategies include air cooling, indirect liquid cooling, phase-change-material cooling, and heat-pipe-based cooling [8–10]. However, as battery power density and charge/discharge rates increase, achieving effective heat removal and temperature uniformity under high thermal loads remains challenging. Immersion cooling has consequently attracted increasing attention because the battery cells are

Copyright: © 2026 by the authors. This is an open access article under the terms and conditions of the Creative Commons Attribution (CC BY) license (https://creativecommons.org/licenses/by/4.0/).
Publisher's Note: Scilight stays neutral with regard to jurisdictional claims in published maps and institutional affiliations.

directly exposed to a dielectric coolant, providing a large heat-transfer area and reducing the thermal resistance associated with indirect cooling interfaces [8,11].

In single-phase immersion cooling, the dielectric coolant remains liquid, and heat is removed primarily by sensible heating and natural or forced convection. Recent studies have demonstrated its potential for improving both battery temperature control and temperature uniformity. Huang et al. [12] integrated finned heat pipes into an immersion-cooling configuration and reported improved heat-dissipation performance with increasing numbers of heat pipes. Liu et al. [13] compared air cooling, static immersion cooling, and forced-flow immersion cooling for NCM811 battery modules and found that immersion cooling improved both module temperature distribution and voltage consistency. Chandrasekaran et al. [14] experimentally investigated a 6S1P cylindrical battery module under single-phase immersion cooling and reported reductions in maximum temperature of approximately 25.3–75.6% compared with natural cooling over discharge rates of 0.5–4C. Wahab et al. [15] further showed that forced single-phase immersion cooling effectively controlled the maximum temperature of a 48-V lithium-ion battery pack under an 8C discharge condition. Similarly, Hu et al. [16] demonstrated that dynamic immersion cooling reduced both the maximum battery-pack temperature and the maximum temperature difference compared with conventional liquid cooling and static immersion cooling. Choi et al. [17] showed that optimizing internal flow paths and heat-conduction structures could further enhance the performance of single-phase immersion cooling under fast-charging conditions.

More recently, Sheng et al. [11] experimentally investigated static and dynamic immersion cooling of a high-capacity lithium-ion battery module over a wide range of ambient temperatures. Their results demonstrated that dynamic immersion cooling could effectively suppress the module temperature rise and maintain temperature uniformity even under elevated ambient-temperature conditions. Li et al. [18] also investigated an FS49-based immersion-cooling system for an 8S1P prismatic $LiFePO_4$ module and reported improved temperature uniformity and reduced state-of-charge inconsistency compared with natural convection. These studies demonstrate the effectiveness of single-phase immersion cooling; however, its heat-removal capability is primarily governed by the coolant's sensible heat capacity and convective transport, which can become limiting as the battery heat load increases.

Two-phase immersion cooling extends the heat-removal capability of immersion systems by utilizing boiling of the coolant and the associated latent heat of vaporization. Once the battery surface temperature approaches the coolant saturation temperature, nucleate boiling can provide substantial heat removal while limiting further increases in battery temperature. Li et al. [19] investigated two-phase immersion cooling for large cylindrical lithium-ion batteries and reported that the battery temperature could be maintained at approximately 34–35 °C. Liu et al. [20] numerically compared two-phase immersion cooling with conventional cold-plate cooling and showed that two-phase immersion cooling resulted in a lower average battery temperature under a 3C discharge condition. Williams et al. [21] experimentally investigated four 26650 $LiFePO_4$ cells under single-phase natural convection and two-phase pool-boiling immersion cooling and reported maximum cell temperature rises of only 1.9 °C and 1.3 °C during 4C discharge and 4C charge, respectively.

Other studies have further demonstrated the applicability of two-phase immersion cooling to different battery configurations and operating conditions. Zhou et al. [22] combined heat pipes with an immersion phase-change liquid, achieving a maximum battery temperature of approximately 47 ± 1 °C while maintaining a module temperature difference of 1.3–2.1 °C. Kureshi et al. [23] investigated n-pentane as a low-cost dielectric coolant and demonstrated effective temperature regulation under cyclic loading and fast-charging conditions. Bai et al. [24] reported that a simplified two-phase immersion-cooling system limited the maximum temperature of a 5P6S battery module to 37.7 °C under 3C discharge and 1C charge cycles. Banerjee et al. [25] numerically examined air, deionized water, and Al_2O_3 nanofluid immersion cooling and demonstrated substantial reductions in battery-pack temperature under a 5.8C discharge condition. More recently, Koucheh et al. [26] systematically compared natural convection, forced-air cooling, cold-plate cooling, single-phase immersion cooling, and two-phase immersion cooling at the battery-pack scale, demonstrating the strong potential for temperature control and uniformity of two-phase immersion cooling.

Although these studies demonstrate the advantages of latent-heat-based cooling under high thermal loads, the performance of two-phase immersion cooling strongly depends on the coolant's thermophysical properties and the resulting boiling behavior. In particular, boiling onset, vapor generation, bubble transport, and local liquid replenishment can affect not only the maximum battery temperature but also the temperature uniformity within the module. Therefore, coolant selection should consider the coupled effects of sensible heat transfer, phase-change heat transfer, and vapor-induced modification of the flow field. Despite the growing number of studies on battery immersion cooling, most previous investigations have focused on a specific coolant, a particular cooling configuration, or a limited range of operating conditions. Systematic cross-coolant comparisons conducted under the same module geometry and common hydrodynamic conditions remain limited, particularly regarding the

coupled relationships among coolant properties, boiling onset, vapor generation, and module temperature uniformity as battery heat loads increase. Consequently, the transition from convection-dominated single-phase cooling to latent-heat-dominated two-phase cooling, as well as the potential deterioration in temperature uniformity caused by excessive vapor accumulation, has not yet been sufficiently clarified.

To address this research gap, the present study establishes a three-dimensional transient numerical model of a lithium-ion battery module using the Volume of Fluid (VOF) method coupled with the Lee phase-change model. Four dielectric coolants—FS49, SF33, Novec 7000, and R141b—are systematically compared at a common Reynolds number, Re = 500, and across different battery discharge rates. The thermal and phase-change characteristics are evaluated using module temperature distribution, average temperature, maximum temperature difference, temperature standard deviation, and gas-phase volume fraction. Particular attention is given to the relationships among coolant boiling characteristics, vapor generation, latent-heat utilization, and temperature uniformity. The results provide a systematic basis for selecting coolant properties and operating conditions for high-power two-phase immersion-cooled battery systems.

2. Geometric Model Construction

The ANR26650M1B cell is considered for the numerical simulation. This type of battery has good specifications, including stable chemical properties, rapid charging, long cycle life, and safety. The specifications of the ANR26650M1B cell are provided in Table 1. The lithium battery module, cooling tank, and coolant area are used as the main computational domains for numerical simulations of heat dissipation efficiency and temperature distributions across different coolants and discharge rates. The battery cells are also arranged in the standard configuration in the cooling tank, and the coolant completely covers the battery surface to simulate the actual immersion cooling operation. The basic specifications of the model are shown in Figure 1. The geometrical parameters considered for the immersion cooling unit are provided in Table 2. In this table, d_i and d_o are the diameters of the inlet and outlet vents, respectively. W_1 is the distance between two adjacent battery cells within the module. W_2 is the distance between the outer surface of the last cell and the inner wall of the module.

Table 1. ANR26650M1B Cell specifications.

Main Characteristics	Value	Unit
Nominal Voltage	3.3	V
Capacity	2.5	Ah
End-of-Discharge Cut-Off Voltage	2.0	V
Energy	8.25	Wh
Gravimetric Energy Density	108.6	Wh/kg
Volumetric Energy Density	239	Wh/L
AC Impedance	6	mΩ
Dimensions	26 × 65	mm
Weight	76	g
Density	2047	kg/m^3
Specific Heat Capacity	1605	J/kg·K
Thermal Conductivity (Axial/Radial)	32/0.15	W/m·K
Operating Temperature	−30~+60	°C

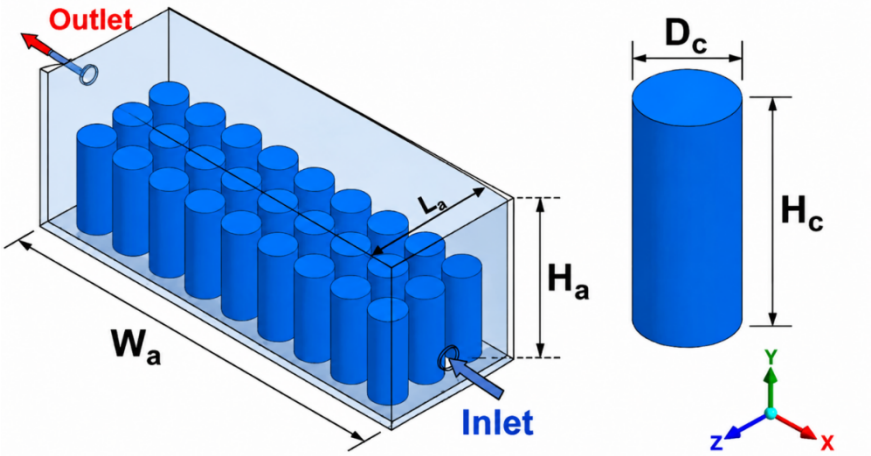


Figure 1. Schematic of the two-phase immersion cooling module.

Table 2. Geometrical parameters considered for the immersion cooling unit.

Parameters	Value (cm)
L_a	10.6
W_a	31.4
H_a	12
D_c	2.6
H_c	6.5
d_i	1.2
d_o	1.2
H_1	5.3
W_1	1
W_2	0.7

3. Mathematical Modeling

For numerical solutions, the governing equations of the flow field are discretized using the Finite Volume Method (FVM). By solving the mass conservation, momentum conservation, energy conservation, and volume fraction transport equations, the distributions of coolant and vapor, as well as the temperature changes around the lithium battery module, can be obtained. The Volume of Fluid (VOF) method is used for the simulation of the boiling, evaporation, and two-phase flow of the coolants after heating on the lithium-ion battery in the cooling module. Since the two-phase immersion cooling investigated in this study is a transient heat-flow problem that varies over time, and the boiling interface continues to form, grow, and break down, a transient solution method is adopted to better capture the actual phase change and flow-field changes. In addition, to reasonably describe the evaporation process of the coolant near the heated surface, this study will use the Lee model as the phase-change mass-transfer model. This model can calculate the mass exchange rate between the liquid and gas phases based on the difference between the local temperature and the saturation temperature, thereby simulating the process of coolant changing from liquid to gas. By integrating the above numerical methods, this simulation can explore how different operating parameters affect the two-phase immersion cooling performance of lithium battery modules and analyze their effects on temperature, temperature uniformity, and overall heat dissipation.

3.1. Volumetric Fluid Method

The VOF model can accurately capture the interface location and its temporal evolution through the solution of the volume-fraction transport equation, which is written as follows:

$$\sum_{q=1}^{n} \alpha_v = 1 \tag{1}$$

For the gas–liquid two-phase flow considered in this work, the formulation can be reduced to a two-component system consisting of a liquid phase and a gas phase, which may be expressed in the following simplified form:

$$\alpha_l + \alpha_v = 1 \tag{2}$$

where α_l and α_v denote the volume fractions of the liquid coolant and the vapor phase, respectively. Within the VOF framework, capturing the evolution of the liquid–vapor interface is achieved by solving a volume-fraction transport equation. For the vapor (gas) phase, the corresponding volume fraction equation can be written as:

$$\frac{1}{\rho_v}\left[\frac{\partial}{\partial t}(\alpha_v \rho_v) + \nabla \cdot (\alpha_v \rho_v \overrightarrow{v_v})\right] = s_v + \sum_{v=1}^{n} (\dot{m}_{lv} - \dot{m}_{vl}) \tag{3}$$

In this expression, ρ_v denotes the vapor density, $\overrightarrow{v_v}$ represents the vapor-phase velocity vector, and s_v is the mass source term associated with the gas phase. The terms $\dot{m}_{lv}$ and $\dot{m}_{vl}$ correspond to the interphase mass transfer rates from liquid to vapor and from vapor to liquid, respectively.

3.2. Lee Model

To model coolant evaporation and condensation during two-phase immersion cooling of lithium-ion battery modules, this work adopts the Lee model as the interphase mass-transfer approach between the liquid and vapor phases [27–29]. In the Lee formulation, the mass-transfer rate for liquid-phase evaporation is:

$$\dot{m}_{lv} = C_{evap}\alpha_l\rho_l\frac{T_l - T_{sat}}{T_{sat}},\ T_l > T_{sat} \tag{4}$$

The mass transfer rate associated with vapor-phase condensation is:

$$\dot{m}_{vl} = C_{cond}\alpha_v\rho_v\frac{T_{sat} - T_v}{T_{sat}},\ T_v < T_{sat} \tag{5}$$

where C_{evap} and C_{cond} denote the phase-change coefficients for evaporation and condensation, respectively; in this work, both are set to 0.1. Here, ρ_l is the liquid density, T_l and T_v are the liquid- and vapor-phase temperatures, and T_{sat} represents the coolant saturation temperature.

3.3. Assumptions

The fundamental assumptions are defined as follows:

- Both the liquid and vapor phases are treated as continuous, incompressible media.
- The liquid and gas phases are assumed to be immiscible.
- Gravitational and surface tension effects are fully incorporated. Thermal radiation is considered negligible.
- The battery is represented as a homogeneous solid with uniform volumetric heat generation. Consequently, internal electrochemical processes and the heterogeneity of the battery's layered internal structure are excluded from the model.
- Thermophysical properties for both the liquid and vapor phases are assumed to remain constant. Furthermore, factors such as coolant aging, chemical decomposition, and the presence of non-condensable gases are disregarded.

3.4. Governing Equations

The governing equations adopted in this study are given as follows:

- Mass Conservation Equation

$$\frac{\partial\rho}{\partial t} + \nabla\cdot(\rho\vec{v}) = 0 \tag{6}$$

where $\vec{v}$ is the fluid velocity vector.

- Volume fraction equations

$$\frac{\partial}{\partial t}(\alpha_v\rho_v) + \nabla\cdot(\alpha_v\rho_v\vec{v}) = \mathrm{S}_v + \dot{\mathrm{m}}_{lv} - \dot{\mathrm{m}}_{vl} \tag{7}$$

$$\frac{\partial}{\partial t}(\alpha_l\rho_l) + \nabla\cdot(\alpha_l\rho_l\vec{v}) = \mathrm{S}_l + \dot{\mathrm{m}}_{vl} - \dot{\mathrm{m}}_{lv} \tag{8}$$

Here, S_v and S_l are the source terms.

- Momentum equation

The momentum equation is:

$$\frac{\partial(\rho\vec{v})}{\partial t} + \nabla\cdot(\rho\vec{v}\vec{v}) = -\nabla P + \nabla\cdot(\mu\nabla\vec{v}) + \rho g + \vec{F} \tag{9}$$

Here, ρ denotes the mixture density, P is the pressure, μ represents the mixture dynamic viscosity, and $\vec{F}$ is the volumetric surface-tension force. The mixture density and viscosity are given by [30]:

$$\rho = \alpha_l\rho_l + \alpha_v\rho_v \tag{10}$$

$$\mu = \alpha_l\mu_l + \alpha_v\mu_v \tag{11}$$

The volumetric surface-tension force is defined by:

$$\vec{F} = \sigma\kappa\nabla\alpha_l \tag{12}$$

$$\kappa = -\nabla \cdot \frac{\nabla \alpha_l}{|\nabla \alpha_l|} \tag{13}$$

In this formulation, σ is the surface-tension coefficient and κ represents the interfacial curvature.

- Energy equation

$$\frac{\partial(\rho C_P T)}{\partial t} + \nabla \cdot \left(\rho \vec{v} C_p T\right) = \nabla \cdot (k \Delta T) + S_h \tag{14}$$

Here, C_p denotes the mixture specific heat capacity at constant pressure, T is the temperature, and $\vec{v}$ is the velocity vector. The parameter k represents the mixture thermal conductivity. S_h is defined by [31]:

$$S_h = q'''_{battery} + \dot{m} L_f \tag{15}$$

In this expression, $q'''_{battery}$ is the volumetric heat generation rate within the battery module, $\dot{m}$ denotes the interphase mass transfer rate due to phase change, and L_f is the latent heat of vaporization of the coolant.

- Battery heat transfer equation

Beyond the fluid domain, the thermal management assessment in this work also examines how heat is generated within the lithium-ion cell and subsequently transported through the battery body. Because the battery surface temperature arises from the combined effects of internal heat generation and heat conduction within the solid, a governing heat-transfer equation for the battery solid region must be established. The transient heat conduction equation of the battery is [32]:

$$\rho_b C_{p,b} \frac{\partial T_b}{\partial t} = \nabla \cdot (K_b \nabla T_b) + q'''_{battery} \tag{16}$$

Here, ρ_b denotes the battery density, $C_{p,b}$ is the specific heat capacity of the battery at constant pressure, T_b represents the battery temperature, K_b is the battery thermal conductivity, and $q'''_{battery}$ is the volumetric heat generation rate within the battery.

The model equation for battery heat generation is [33]:

$$\dot{Q}_{battery} = I_b(E_{oc} - U) - I T_b \frac{\mathrm{d}E_{oc}}{\mathrm{d}T_b} \tag{17}$$

In this expression, I_b denotes the battery current, E_{oc} is the open-circuit voltage, and U represents the actual operating voltage. To introduce the total heat generation rate into the heat conduction equation, the present study further converts it into an equivalent volumetric heat generation rate, which can be written as:

$$q'''_{battery} = \frac{\dot{Q}_{battery}}{V_b} \tag{18}$$

Here, V_b denotes the battery volume.

3.5. Boundary Conditions

The boundary condition setup in this study mainly comprises three parts: the fluid domain, the battery module, and the single-phase and two-phase models. In the fluid domain, to reduce the impact of initial field discontinuities on the solution, the battery and coolant temperatures at the initial calculation time were both set to the ambient temperature of 30 °C, and the initial flow field was assumed to be static. For material selection, aluminum was chosen for the cooling module structure, primarily due to its excellent thermal conductivity, low density, and ease of processing. In terms of simulation conditions, a flow-boiling boundary setting was adopted. Heat removal was achieved primarily by the cooling medium flowing out of the outlet to maintain thermal equilibrium. The battery module was treated as a homogeneous solid region, with an internal volumetric heat source applied to describe the heating characteristics during charging and discharging. In the two-phase model, in addition to defining the flow field boundary, the initial distributions of the gas and liquid phases needed to be specified to describe the evaporation behavior and mass transfer during phase transitions on the cell surface. Boundary conditions and material properties are shown in Tables 3 and 4. Coolant parameters are shown in Table 5.

Table 3. Boundary conditions.

Items	Boundary Condition
Inlet	Volume flow rate
Outlet	Pressure outlet
Battery Surface	Coupled wall
Tank Wall Surface	Adiabatic/No-slip surface

Table 4. Material properties.

Parameter	Density	Specific Heat	Thermal Conductivity
	kg/m^3	J/kg·K	W/m·K
Battery	2047	1605	Axial: 32 Radial: 0.15
Aluminum	2719	871	202.4

Table 5. Coolant parameters [34–36].

Property	Unit	Novec7000	FS49	SF33	R141b
Boiling point	°C	34	49	33.4	32.05
Liquid density	kg/m^3	1400.6	1601.4	1615	1220.03
Vapor density	kg/m^3	7.722	6.645	7.5	4.86
Liquid specific heat	J/kg·K	1300.2	1102.9	1200	1163.6
Vapor specific heat	J/kg·K	1005	900	880	810.8
Surface tension	N/m	0.0124	0.0108	0.0127	0.0173
Liquid thermal conductivity	W/m·K	0.0749	0.059	0.08	0.0887
Vapor thermal conductivity	W/m·K	0.026	0.013	0.012	0.0104
Liquid viscosity	kg/m·s	0.00045	0.00064	0.00038	0.000377
Vapor viscosity	kg/m·s	0.00001	0.000011	0.00001	0.00000941
Liquid standard state enthalpy	J/kg·mol	0	0	0	0
Vapor standard state enthalpy	J/kg·mol	2.84×10^7	2.78×10^7	2.72×10^7	2.61×10^7

3.6. Performance Evaluation Indicators

Since two-phase immersion cooling involves the flow field, temperature field, gas-liquid interface evolution, and phase-change behavior, its transient solutions often exhibit strong time dependence. Therefore, it is not enough to judge convergence solely by the residuals. This study further selects monitoring parameters with physical significance as an auxiliary basis for judging the stability and reliability of the numerical solution. Therefore, in addition to monitoring the residuals of each control equation during the solution process, the battery maximum temperature ($T_{\max}$), module average temperature (T_{avg}), module maximum temperature difference (ΔT_{max}), and gas phase volume fraction (α_v) are also monitored simultaneously. Among them, the maximum temperature is used to evaluate the system's thermal safety, the maximum temperature difference reflects the uniformity of the module temperature distribution [35], and the gas-phase volume fraction can serve as a basis for analyzing local boiling and gas-liquid interface evolution [31]. Based on the time history of the above physical quantities as an auxiliary basis for convergence judgment, when the changes of each monitoring parameter tend to be stable within a continuous time step, and the residuals simultaneously meet the convergence conditions, the transient solution result can be regarded as having good numerical stability and physical reliability. The equations for each index are defined here:

- Maximum temperature difference ($\Delta T_{\max}$):

$$\Delta T_{\max} = T_{\max} - T_{\min} \tag{19}$$

This indicator represents the temperature difference between the module's maximum and minimum temperatures. A smaller maximum temperature difference indicates a more uniform temperature distribution across the module. If the temperature difference becomes too large, it suggests uneven cooling.

- Temperature standard deviation (σ_T):

$$\sigma_T = \sqrt{\frac{1}{N}\sum_{i=1}^{N}\left(T_i - T_{avg}\right)^2} \tag{20}$$

This parameter describes how the temperatures of all batteries are distributed around the mean value. T_i represents the average temperature of the lithium battery, T_{avg} is the mean temperature of the module, and N denotes the total number of batteries. A lower temperature standard deviation means better thermal uniformity. In contrast, a higher temperature standard deviation implies a greater non-uniformity.

- Gas phase volume fraction (α_v):

$$\overline{\alpha_v} = \frac{1}{V_f}\int_{V_f} \alpha_v \, dV \tag{21}$$

The vapor volume fraction indicates the extent of vapor formation throughout the fluid domain. However, higher vapor generation does not automatically translate into better cooling performance. Therefore, it should be evaluated alongside the temperature field distribution and the resulting temperature variations to draw a reliable overall conclusion.

4. Numerical Method

This study employs the PISO (Pressure-Implicit with Splitting of Operators) algorithm to handle pressure–velocity coupling. As a member of the SIMPLE family, PISO is well-suited for transient simulations. To enhance solution stability and improve the accuracy of pressure correction, Neighbor Correction and Skewness Correction are also incorporated into the PISO scheme. The relevant discretization scheme settings used in this study are provided in Table 6. The relaxation factors for pressure and momentum are specified as 0.3 and 0.7, respectively, in order to maintain a balance in the stability of the pressure–velocity coupling process. The volume-fraction relaxation factor is set to 0.5 to reduce the impact of gas–liquid interface oscillations on the numerical results in two-phase flow simulations. In the field of lithium-ion battery thermal management, it is well established that the optimal time step for transient simulations depends on both the model's scale and its physical complexity. In a study focused on single-phase immersion cooling of a 26650 battery, Williams et al. [37] evaluated three distinct time steps, 1 s, 0.1 s, and 0.01 s, to determine their impact on model convergence. Their findings indicated that reducing the time step from 1 s to 0.1 s and 0.01 s resulted in minimal variations in the average surface temperature, with differences of only 0.01% and 0.03%, respectively. Based on these results, a time step of 0.1 s was selected for their subsequent simulations. Williams et al. [21] also conducted an experimental investigation of a module comprising four 2.5 Ah ANR26650M1B 26650 lithium-ion cells. They reported that once two-phase immersion cooling was achieved using Novec 7000 as the coolant, pronounced, vigorous boiling occurred on the battery surfaces, leading to a substantial enhancement in heat transfer compared with single-phase conditions. Their results further indicated that two-phase immersion cooling simulations require a finer time step than single-phase models in order to accurately capture the transient behavior of the gas–liquid interface. To verify the suitability of the time step, the variation in the average battery temperature under different time-step settings was further compared. We performed a sensitivity analysis across three time steps: 1 s, 0.5 s, and 0.1 s, with the 0.1 s setting as the baseline for comparison. Data from Table 7 indicate that with a 1 s time step, the deviations from the 0.1 s reference peaked at the end of the discharge phase (500 s), with errors ranging from 0.12% to 0.73%. By refining the step size to 0.5 s, the relative error was notably reduced; the peak error dropped to 0.26%, and at several instances, the predicted values aligned almost perfectly with the baseline (approaching 0% error). This convergence demonstrates that a 0.5 s time step is sufficiently robust to resolve the batteries' transient thermal response with high accuracy (error < 0.3%). Consequently, we selected 0.5 s as the optimal time step, as it provides the necessary balance between computational efficiency, simulation stability, and the accurate resolution of the gas–liquid interface.

Table 6. Relevant discretization scheme settings used in this study.

Category	Parameter	Set Value
Spatial discretization	Gradient	Least Squares Cell Based
	Pressure	PRESTO!
	Momentum	Second Order Upwind
	Volume fraction	Compressive
	Energy	Second Order Upwind

Table 7. Calculation of relative error of time step.

Time (s)	t = 1 s		t = 0.5 s		t = 0.1 s
	T (°C)	Relative Error (%)	T (°C)	Relative Error (%)	T (°C)
50	31.22	0.65	31.02	0	31.02
100	32.07	0.16	32.00	0.06	32.02
150	32.99	0.12	32.93	0.06	32.95
200	33.94	0.3	33.83	0.03	33.84
250	34.82	0.4	34.68	0	34.68
300	35.65	0.48	35.50	0.06	35.48
350	36.44	0.52	36.28	0.08	36.25
400	37.20	0.6	37.03	0.14	36.98
450	37.93	0.66	37.75	0.19	37.68
500	38.63	0.73	38.45	0.26	38.35

In this work, the residual convergence thresholds for continuity and volume fraction are prescribed as 10^{-4}, while those for momentum and energy are tightened 10^{-6}, following the recommendations of the aforementioned studies.

4.1. Mesh Model

In this study, the mesh model was generated primarily using a hybrid meshing strategy. This method primarily uses tetrahedral meshes, supplemented by hexahedral, wedge, and pyramid meshes as transitional elements. This enhances the mesh adaptability and overall computational stability of the complex geometric model. The relatively regular, large-volume fluid regions inside the tank can be divided using a tetrahedral core mesh, while different mesh types are used for transitions on the cylindrical battery surface and at complex geometric interfaces, thereby improving overall mesh quality and numerical stability. Since the geometric model in this study includes a cuboid cooling tank and multiple cylindrical batteries with complex geometries, a hybrid mesh was used for discretization, effectively handling curved surfaces and areas in contact with multiple objects. In terms of mesh configuration, a hybrid mesh is primarily used in the fluid region to improve overall flow-field calculation efficiency, while the battery body is meshed according to its cylindrical geometry, allowing a clear description of the internal heat-conduction path and improving the accuracy of the temperature-distribution simulation. Furthermore, to enhance the analytical capabilities for the flow field, heat transfer behavior, and phase transition region around the battery, this study refines the mesh in the battery region to better capture velocity and temperature gradients, as well as boiling phase transition phenomena. The overall mesh generation diagram is shown in Figure 2.

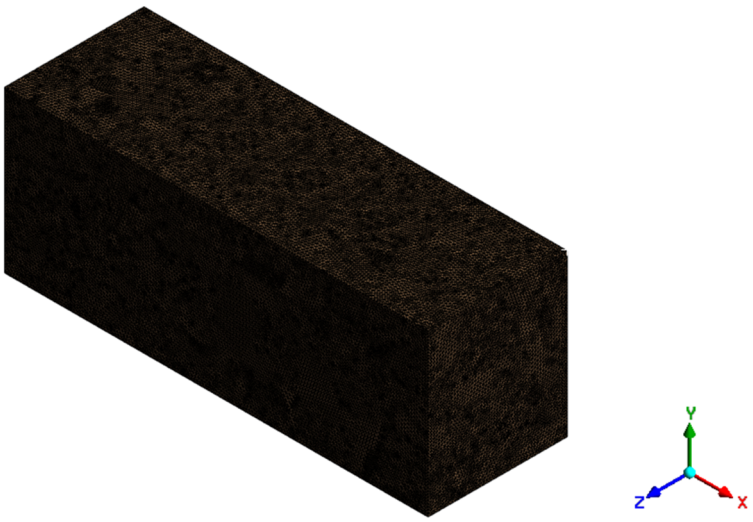


Figure 2. Overall mesh generation diagram of two-phase immersion type.

This study sets the minimum mesh size to 0.025 mm. To accurately capture the flow-field boundary characteristics and phase-change heat-transfer phenomena, face sizing was used to refine the mesh at the coolant inlet, outlet, and battery surface. Body sizing was also applied to the battery itself to enhance analytical capabilities for internal heat generation and changes in conduction. These local mesh optimization strategies effectively improve the mesh distribution in specific regions and significantly enhance the overall mesh quality. Since the two-phase immersion cooling model in this study needs to analyze the impact of near-wall phase-change heat

transfer on the overall temperature field, more elements are required during mesh generation to capture its geometric characteristics and near-wall flow behavior. This improves the resolution of the boundary layer mesh and ensures the convergence and accuracy of the numerical solution. The final generated two-phase model has a total of 6,251,435 meshes, with a minimum orthogonal quality of 0.282. Quality checks show that all mesh parameters are within a reasonable range, with no significant distortion or anomalies, and fully meet the requirements for subsequent high-precision numerical simulations. The temperature variation diagram for grid independence analysis is shown in Figure 3. The simulation results indicate that as the mesh element size decreases from 6 mm to 2 mm, the values of key parameters at monitored locations stabilize, suggesting that the numerical solution is converging and the effect of mesh density has become negligible. Using the finest mesh (2 mm) as the reference, reducing the grid size from 4 mm to 3 mm yielded a 10.04% error, whereas the transition from 3 mm to 2 mm resulted in a much smaller error of 3.32%. This confirms that the model has reached grid independence, with localized parameters showing minimal variation. Therefore, a mesh size of 3 mm was chosen for subsequent analyses, striking an effective balance between computational cost and simulation fidelity.

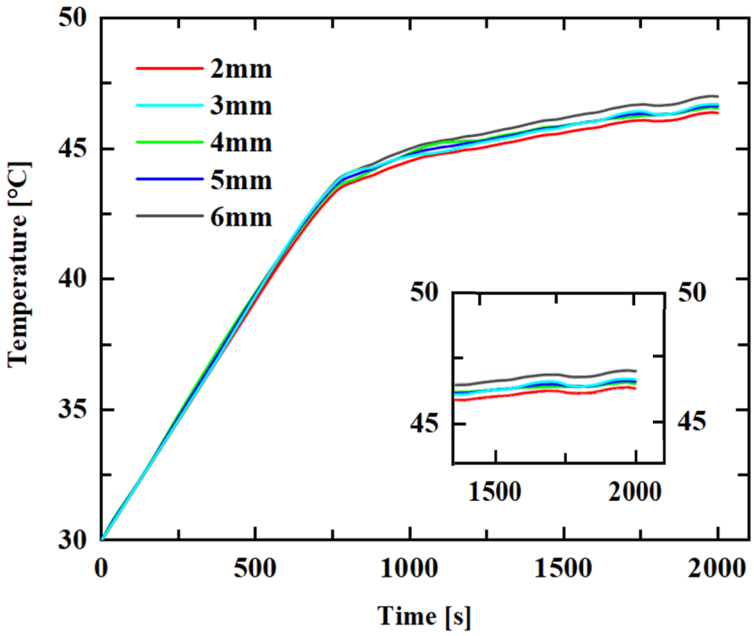


Figure 3. Mesh independence analysis results.

4.2. Validation

To verify the applicability of the LFP battery module model established in this study under two-phase immersion cooling conditions, this study further selects the experimental study by Williams et al. [21] as the benchmark for comparison. The study takes 26650 LFP battery as the object and completely immerses the battery in coolant with an initial temperature of 33 °C. The temperature of the cooling water in the upper copper coil is 15 °C. The study explores the thermal behavior of two-phase immersion cooling. The study is tested at discharge rates of 1C and 4C and explores the influence of battery spacing on the module's maximum temperature and temperature uniformity to evaluate the cooling effect of two-phase phase-change heat dissipation on the thermal management of the battery module. Based on the system architecture and boundary conditions reported in the literature, this study establishes a corresponding two-phase immersion-cooling numerical model, as shown in Figure 4. In the simulation, a 1S4P 26650 LFP battery module is placed in a Novec 7000 immersion-cooling environment, and a two-phase heat-dissipation mechanism is established with a coolant temperature of 33 °C. The condenser's cooling reflux effect is also considered to simulate the pool boiling cooling process in the experiment. The battery pack's volumetric heat generation rate at a fixed discharge rate is analyzed.

Figure 5 and Table 8 present the temperature-rise trends for the simulation and experimental results from the literature. As shown in the figure and table, the temperature rise trend obtained from the simulation with DOD is roughly consistent with experimental results reported in the literature, indicating that the model in this paper can reasonably describe the phase-change heat-dissipation process of the battery module. The error analysis in the table shows that the relative errors at each measurement point are all within 6%, with a maximum deviation of 5.08%.

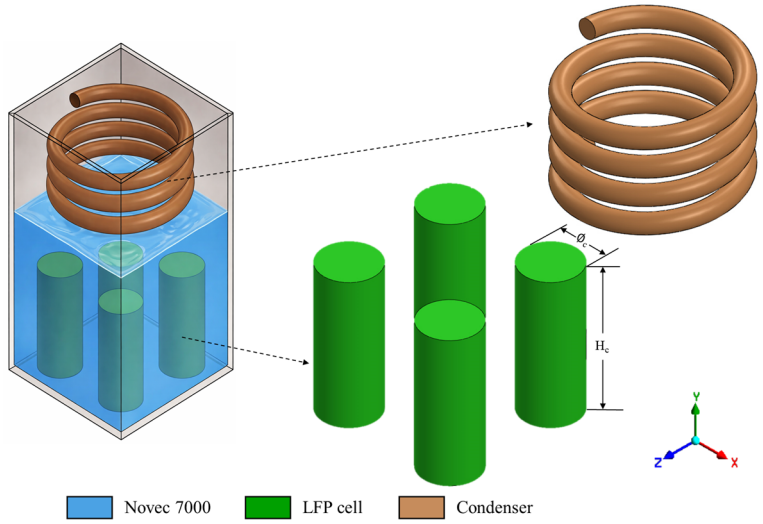


Figure 4. Schematic diagram of the two-phase immersion cooling verification model.

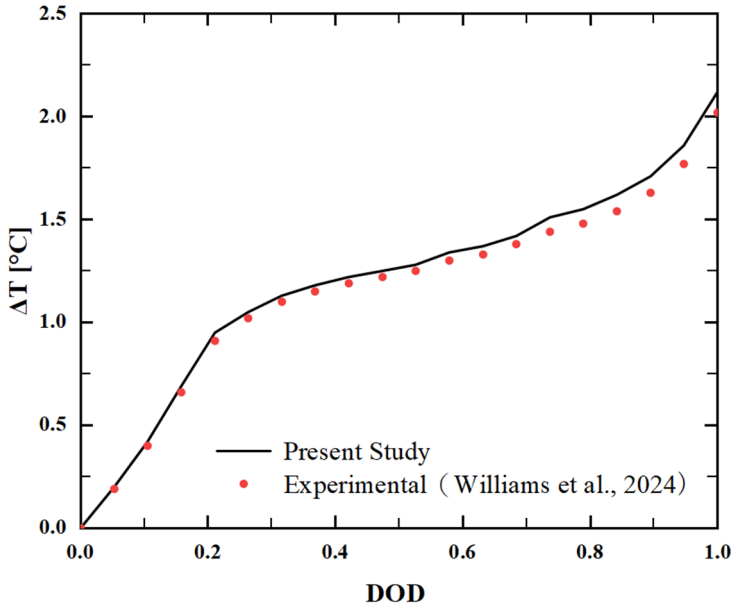


Figure 5. Comparison of battery temperature rise between simulation and literature experimental results [21].

Table 8. Comparison of battery temperature rise and relative error between simulation and literature experimental results.

DOD	Numerical Temperature (°C)	Experimental Temperature (°C)	Relative Error (%)
0	0	0	0
0.11	0.42	0.40	5.00
0.21	0.95	0.91	4.40
0.32	1.13	1.10	2.73
0.42	1.22	1.19	2.52
0.58	1.34	1.30	3.08
0.68	1.42	1.38	2.90
0.79	1.55	1.48	4.73
0.95	1.86	1.77	5.08
1.00	2.12	2.02	4.95

5. Results and Discussion

This section, under a fixed Reynolds number condition (Re = 500), explores the impact of different discharge rates on the thermal management performance of a two-phase immersion cooling module. Since the discharge rate determines the heat generated by the battery module, changes in the discharge rate not only affect the module's average and maximum temperatures but also whether the coolant can effectively reach the boiling initiation

conditions, thereby altering the gas-liquid phase transition behavior and temperature uniformity. The following analysis will examine the module's temperature distribution, average temperature, maximum temperature difference, temperature standard deviation, and gas phase volume fraction results.

As shown in Figures 6–9 and Tables 9–12, as the discharge rate increases from 3C to 6C and 9C, the amount of heat generated per unit time in the battery module also increases. This indicates that a higher discharge rate increases the heat generated by the battery module, resulting in a higher heat load for the coolant to remove. The average temperature, maximum temperature difference, and temperature standard deviation of the module all show an upward trend, and the temperature distribution is significantly less uniform. As shown in the battery module temperature distribution diagram, under the low heat load of 3C discharge rate, the surface color of the modules using SF33, Novec 7000, and R141b is mainly dark blue to cyan, indicating that these coolants can suppress the temperature rise through a stable nuclear boiling mechanism at 3C discharge rate. In contrast, the surface color of the FS49 module is already a lighter cyan, indicating a higher average temperature under single-phase sensible-heat exchange. Therefore, it can be seen that SF33, Novec 7000, and R141b coolants have better temperature rise control at 3C discharge rate, with average temperatures of 35.17 °C, 36.03 °C, and 34.13 °C respectively, and their temperature standard deviations are all within 1.5 °C. Compared with FS49, the heat flux has not reached the saturation point, and it is still in a single-phase forced-convection state; therefore, its average temperature is 43.88 °C, and its temperature standard deviation is 3.35 °C. Although the temperature is significantly higher than that of the other two two-phase coolants, it is still within a safe range.

At a 6C discharge rate, coolants exhibiting phase change demonstrate significant cooling benefits. Using FS49's average temperature of 51.18 °C as a baseline, Novec 7000 and SF33, phase-change coolants, reduced the average temperature to 38.98 °C and 37.98 °C, respectively, by generating a gas-phase volume fraction over 0.5, with temperature uniformity also within 3 °C. R141b, with a gas phase generation of approximately 0.7, is the highest among the four coolants, exhibiting superior heat dissipation capabilities, with an average temperature of only 37.3 °C, a 27.1% reduction compared to FS49. Data analysis confirms that at a 6C discharge rate, two-phase coolants effectively suppress temperature rise and maintain a stable temperature field through latent heat of vaporization, thereby improving the thermal management performance of the battery module. Furthermore, Tables 9–12 also show that when the discharge rate increases from 3C to 6C, the increase in battery heat load significantly widens the performance gap between single-phase and two-phase cooling technologies. FS49, unable to undergo phase change under 6C conditions, saw its average temperature rise from 43.88 °C to 51.18 °C, a temperature increase of 16.6%. This reflects the growing limitations of single-phase sensible-heat exchange under high heat loads. In contrast, coolants Novec 7000, SF33, and R141b, which have triggered phase change and utilized latent heat of vaporization for heat dissipation, effectively suppressed temperature rises, with reductions of 8.2%, 8.0%, and 9.3%, respectively. Data shows that the temperature rise of the coolant that has triggered phase change is only about half that of the coolant still in the single-phase stage (FS49). Regarding temperature uniformity, although the increased discharge rate leads to a more significant phase change, and the generation and detachment of bubbles increase the temperature standard deviation of the two-phase coolant from 1.05–1.32 °C at 3C to 2.37–2.55 °C at 6C, compared to FS49 where the maximum temperature difference rises rapidly by nearly 21 °C due to severe heat accumulation, the two-phase coolant can still stably control the maximum temperature difference within 8.5 °C. This phenomenon not only demonstrates that the two-phase phase change mechanism can effectively mitigate the overall temperature rise trend during high-rate discharge, but also prevents the formation of severe local hot spots, thereby improving the thermal management reliability of the module under drastic increases in heat load.

Significant performance differences were observed under extremely high load conditions, with the discharge rate increasing to 9C. Due to its higher saturation temperature, the FS49 exhibited a vapor phase fraction of 0 even with a dramatic temperature rise on the battery surface at 9C. This indicates that the system relies entirely on sensible heat exchange, resulting in an average temperature increase to 58.31 °C, approximately 32.9% higher than at 3C. The temperature distribution shows large areas of yellow and orange-red on the module surface, indicating that the purely sensible-heat-exchange mode is unable to effectively suppress heat accumulation under high heat flux and that the battery is approaching the critical value of its safe operating temperature. Coolants that undergo phase-change mechanisms exhibit excellent temperature-control capabilities through rapid vaporization. The gas-phase fractions of Novec 7000, SF33, and R141b increase to 0.79, 0.78, and 0.85, respectively, indicating highly active phase change. While the overall temperature rise remains significantly lower than in the single-phase stage, the standard deviation of temperature also increases to approximately 4 °C. This suggests that although boiling can reduce the overall temperature during high-rate discharge and the generation of numerous bubbles provides substantial latent heat of vaporization, the intense gas-liquid interaction and localized bubble accumulation inevitably cause flow-field disturbances, leading to increased temperature differences between individual cells. However, even though the uniformity of the phase-change mechanism deteriorates slightly under extreme loads,

it still significantly reduces the temperature-rise trend compared to pure sensible-heat exchange. Therefore, the design focus of two-phase immersion cooling under high-rate operation is on how to reliably trigger the phase change mechanism while simultaneously eliminating the negative impact of bubble accumulation on temperature uniformity, to maintain the module's overall thermal management reliability.

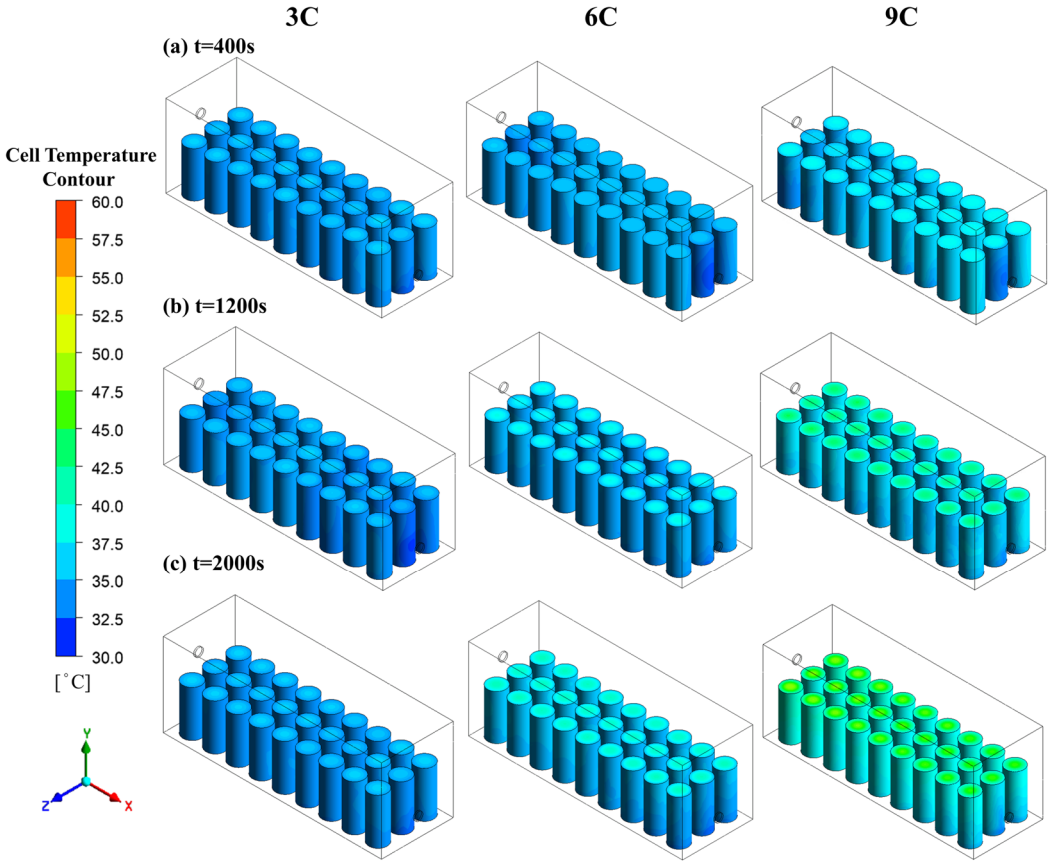


Figure 6. Temperature distribution of SF33 module at Re = 500: (**a**) t = 400 s; (**b**) t = 1200 s; (**c**) t = 2000 s.

Table 9. Module performance indexes of SF33 at different times with Re = 500.

Index	Unit	t = 400 s			t = 1200 s			t = 2000 s		
		3C	6C	9C	3C	6C	9C	3C	6C	9C
ΔT_{max}	°C	1.88	2.7	4.21	4.03	5.63	9.8	3.56	7.15	13.16
T_{avg}	°C	32.81	34.55	36.95	35.04	37.01	40.20	35.17	37.98	42.72
α_v	-	0	0	0.0001	0.0013	0.27	0.51	0.17	0.57	0.78
σ_T	°C	0.09	0.33	0.7	0.87	1.98	3.46	1.05	2.37	4.06

Table 10. R141b module performance indexes at different times with Re = 500.

Index	Unit	t = 400 s			t = 1200 s			t = 2000 s		
		3C	6C	9C	3C	6C	9C	3C	6C	9C
ΔT_{max}	°C	1.3	1.98	3.82	3.09	6.11	11.12	3.59	8.15	14.98
T_{avg}	°C	32.3	33.93	35.39	33.78	36.05	39.65	34.13	37.3	43.5
α_v	-	0	0.0006	0.058	0.15	0.46	0.63	0.387	0.7	0.85
σ_T	°C	0.11	0.48	1.3	0.94	2.09	3.74	1.14	2.42	4.05

Table 11. Module performance indexes of FS49 at different times with Re = 500.

Index	Unit	t = 400 s			t = 1200 s			t = 2000 s		
		3C	6C	9C	3C	6C	9C	3C	6C	9C
ΔT_{max}	°C	9.58	10.93	11.4	14.16	15.2	18.02	15.51	20.94	25.75
T_{avg}	°C	36.77	38.57	40.13	41.29	46.39	51.36	43.88	51.18	58.31
α_v	-	0	0	0	0	0	0	0	0	0
σ_T	°C	0.6	0.45	0.56	2.4	2.03	2.46	3.35	3.3	3.74

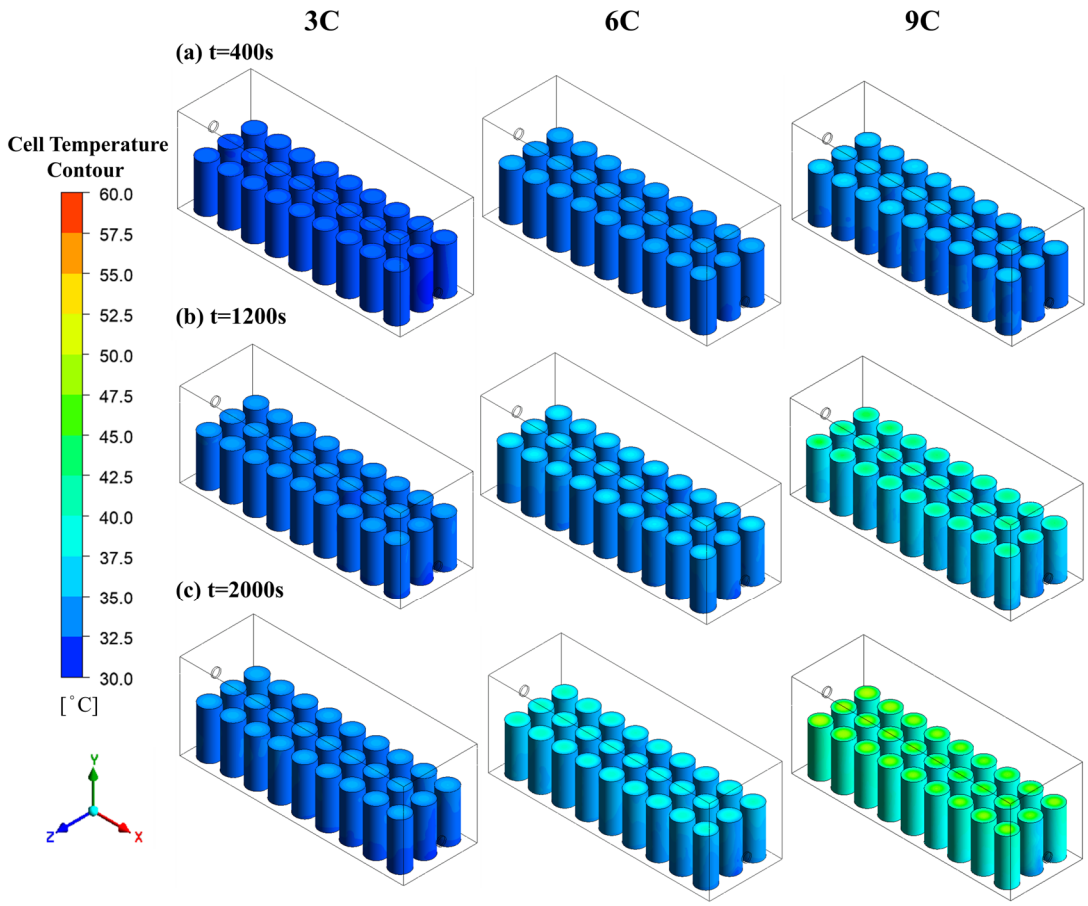


Figure 7. Temperature distribution of R141b module at Re = 500: (**a**) t = 400 s; (**b**) t = 1200 s; (**c**) t = 2000 s.

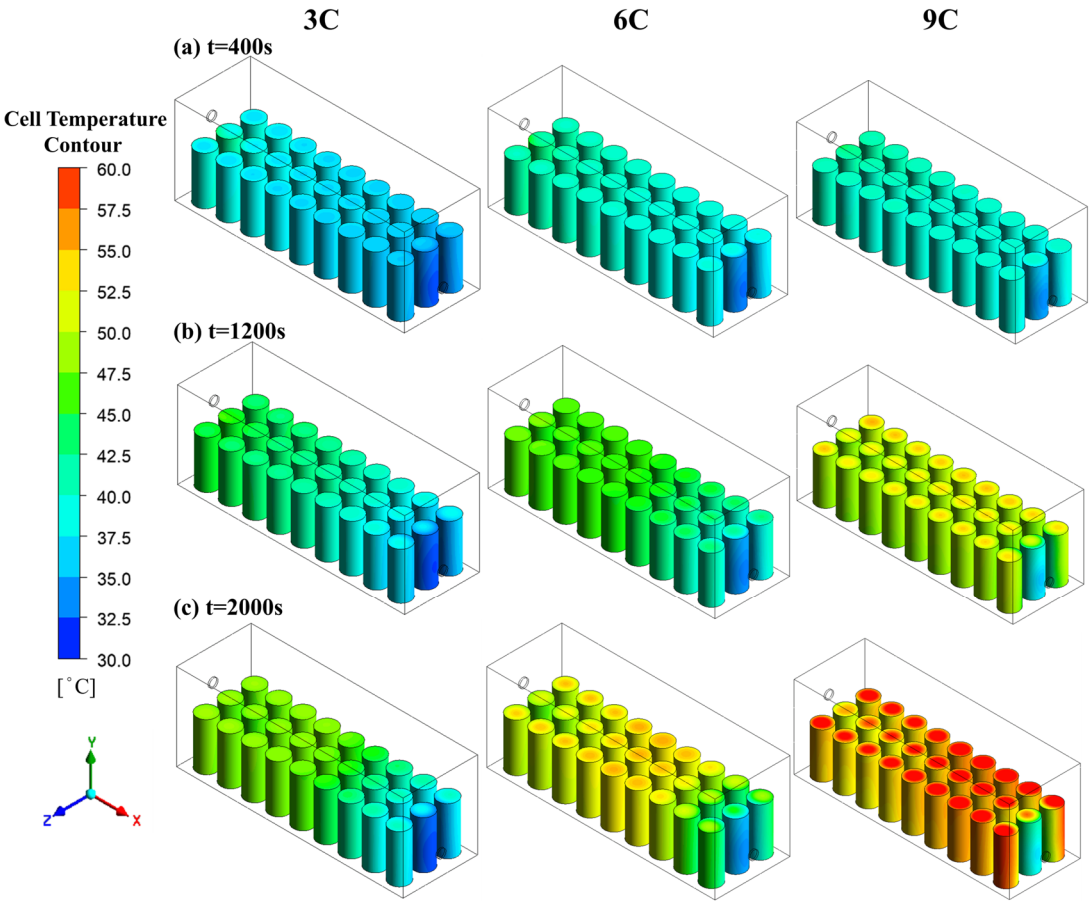


Figure 8. Temperature distribution of FS49 module at Re = 500: (**a**) t = 400 s; (**b**) t = 1200 s; (**c**) t = 2000 s.

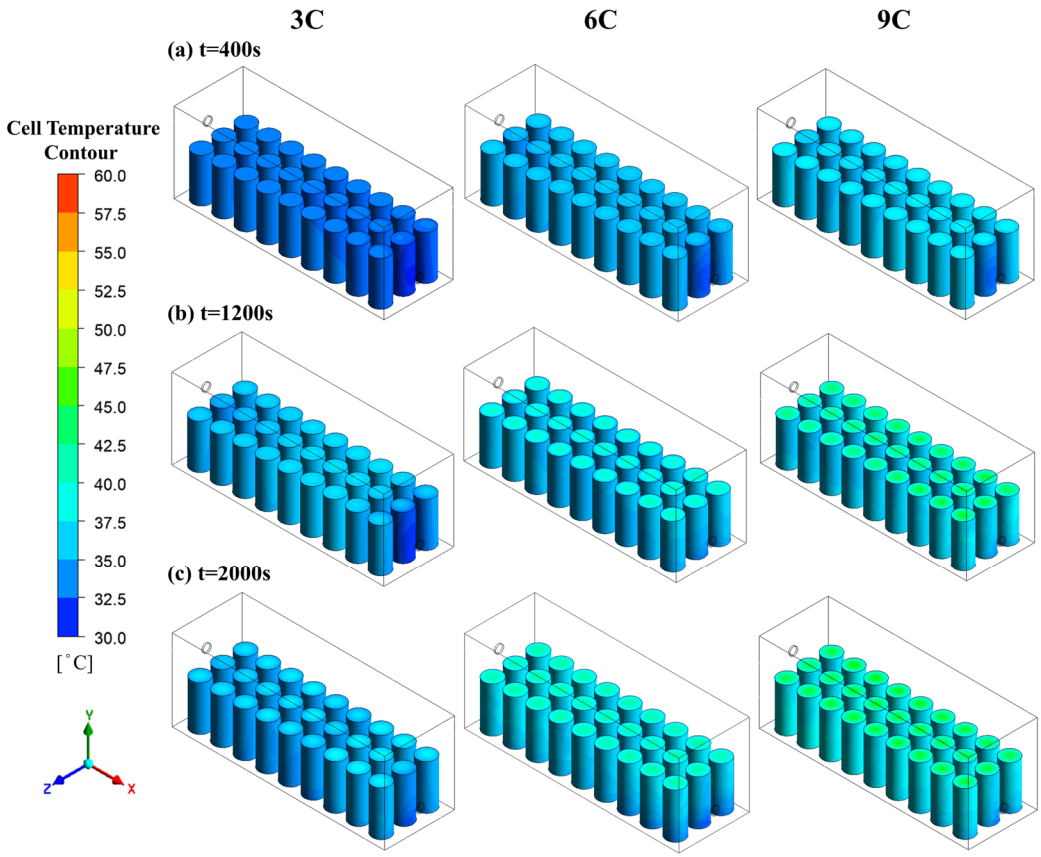


Figure 9. Temperature distribution of Novec 7000 module at Re = 500: (**a**) t = 400 s; (**b**) t = 1200 s; (**c**) t = 2000 s.

Table 12. Novec7000 module performance indexes at different times with Re = 500.

Index	Unit	t = 400 s			t = 1200 s			t = 2000 s		
		3C	6C	9C	3C	6C	9C	3C	6C	9C
ΔT_{max}	°C	2.18	2.89	4.36	5.03	6.48	10.42	5.68	8.37	10.93
T_{avg}	°C	33.03	34.77	36.88	35.79	37.92	40.8	36.03	38.98	41.57
α_v	-	0	0	0	0.00003	0.21	0.5	0.015	0.59	0.79
σ_T	°C	0.09	0.29	0.63	0.66	2.18	3.74	1.32	2.55	3.77

From the visual gas-phase volume-fraction distribution diagrams (Figures 10–13), it can be observed that the discharge rate determines the total amount of gas generated and also changes the evolution pattern and the flow-field structure of bubbles. Under the low heat load of 3C, the onset of nucleate boiling (ONB) of the coolant with phase change capability is significantly delayed. Bubbles are primarily distributed as discrete, point-like particles on the surfaces of the middle and rear sections of the battery in the later stage of discharge, exhibiting a mild, trace nucleation state. When the discharge rate is increased to 6C, the nucleation time is significantly advanced by about 200–500 s. The bubbles are then driven by buoyancy to detach from the wall and are mainly distributed in the narrow flow-channel gaps between the batteries and the confluence area above the module. If the distribution pattern at the same time point is further analyzed, the gas phase occupancy rate in the space increases significantly with the increase of the discharge rate. When the discharge rate is 9C, the system boils violently and completely at t = 1000 s, with numerous bubbles emerging; at t = 1200 s, significant gas-phase congestion occurs at the top of the system. While this extreme spatial saturation provides a substantial latent-heat-of-vaporization benefit in suppressing the maximum temperature rise, the excessively accumulated gas clouds essentially occupy the cross-sectional area of the flow channel and obstruct the liquid-phase return path, making it difficult for the coolant to effectively enter the narrow flow channel for heat replenishment. This gas-phase barrier effect disrupts local convective stability, thereby explaining why the temperature gradient between cells increases at extremely high rates. In summary, a moderate heat load can reliably trigger phase change and optimize the flow field and temperature uniformity, but under extremely high loads, excessively dense bubbles will hinder the return of the liquid phase and lead to increased local temperature differences. Therefore, the design of a two-phase immersion cooling system must balance the benefits of latent heat of vaporization against the adverse effects of bubble accumulation on the flow field.

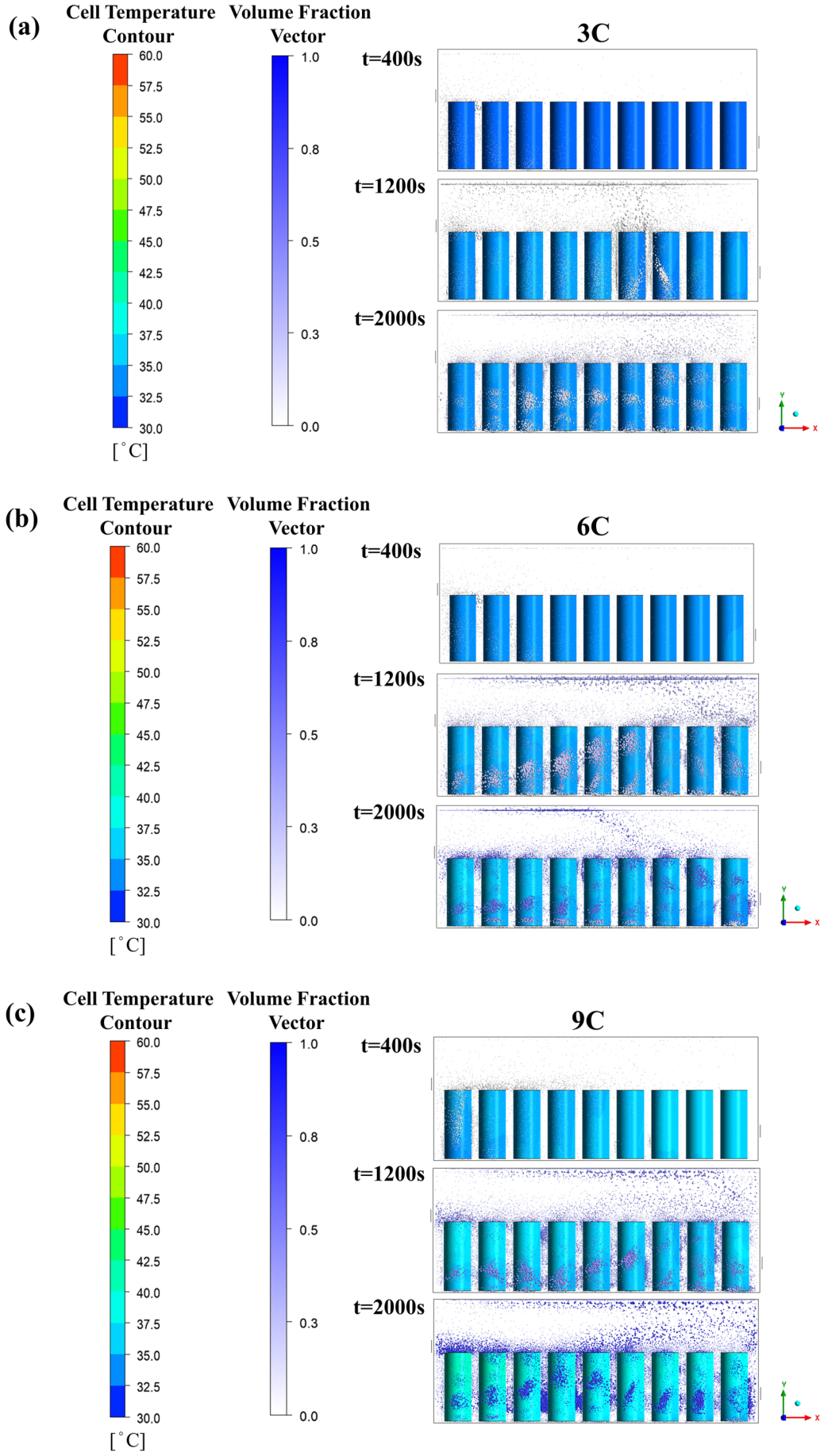


Figure 10. Gas-liquid phase distribution of SF33 module at different times under two-phase immersion cooling. (**a**) 3C, (**b**) 6C, (**c**) 9C.

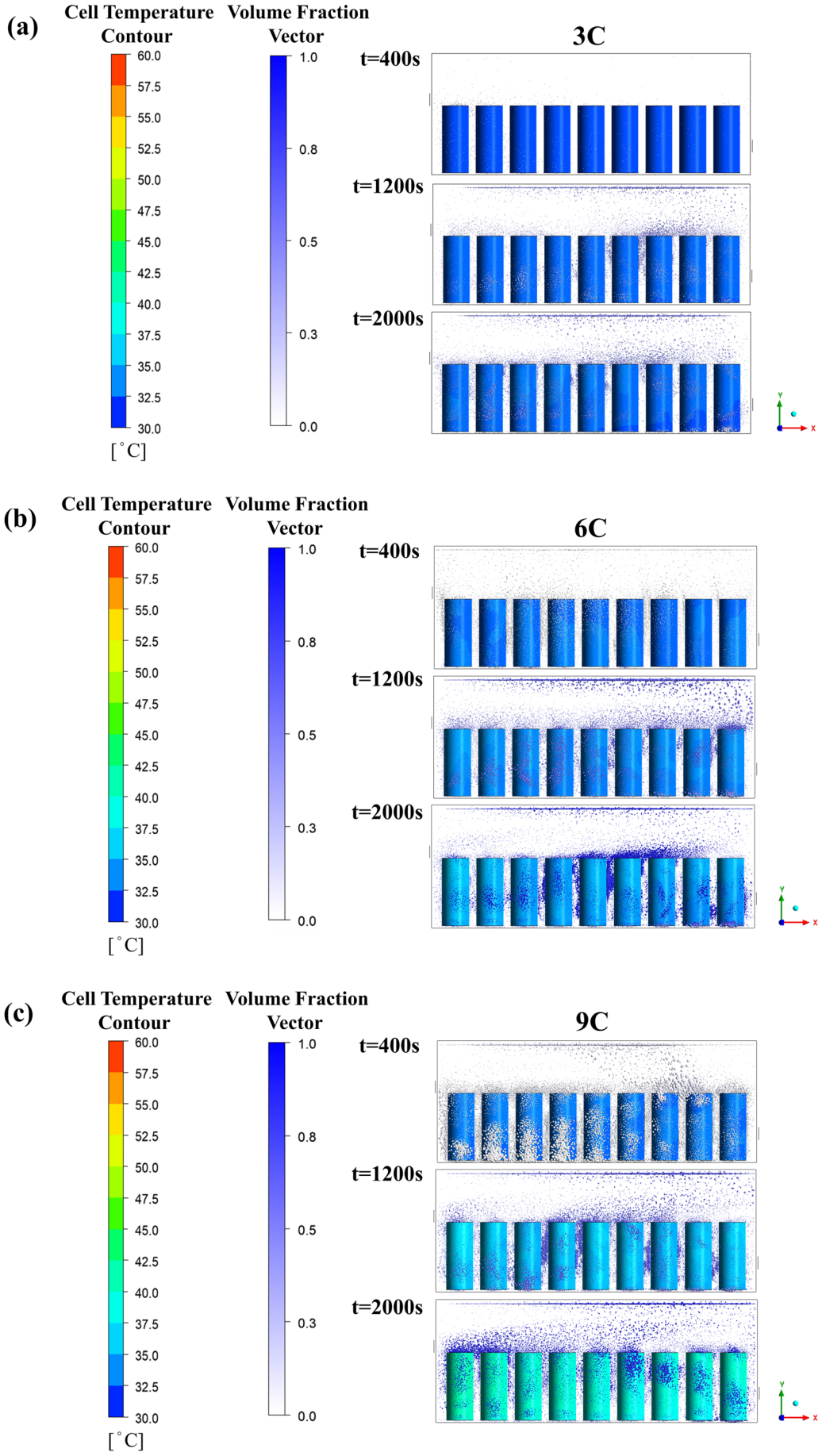


Figure 11. Gas-liquid phase distribution of R141b module at different times under two-phase immersion cooling. (**a**) 3C, (**b**) 6C, (**c**) 9C.

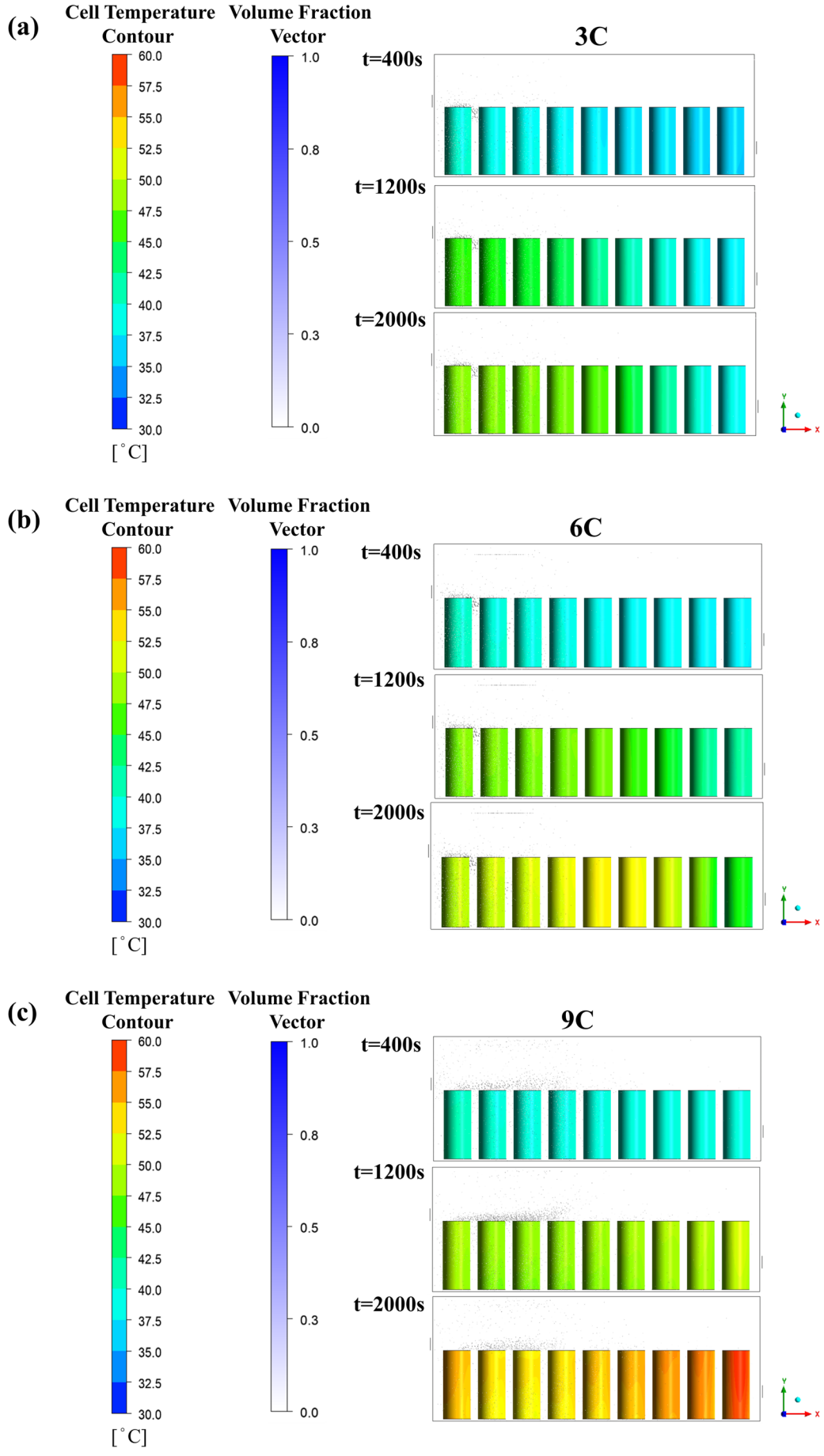


Figure 12. Gas-liquid phase distribution of the FS49 module at different times under two-phase immersion cooling. (**a**) 3C, (**b**) 6C, (**c**) 9C.

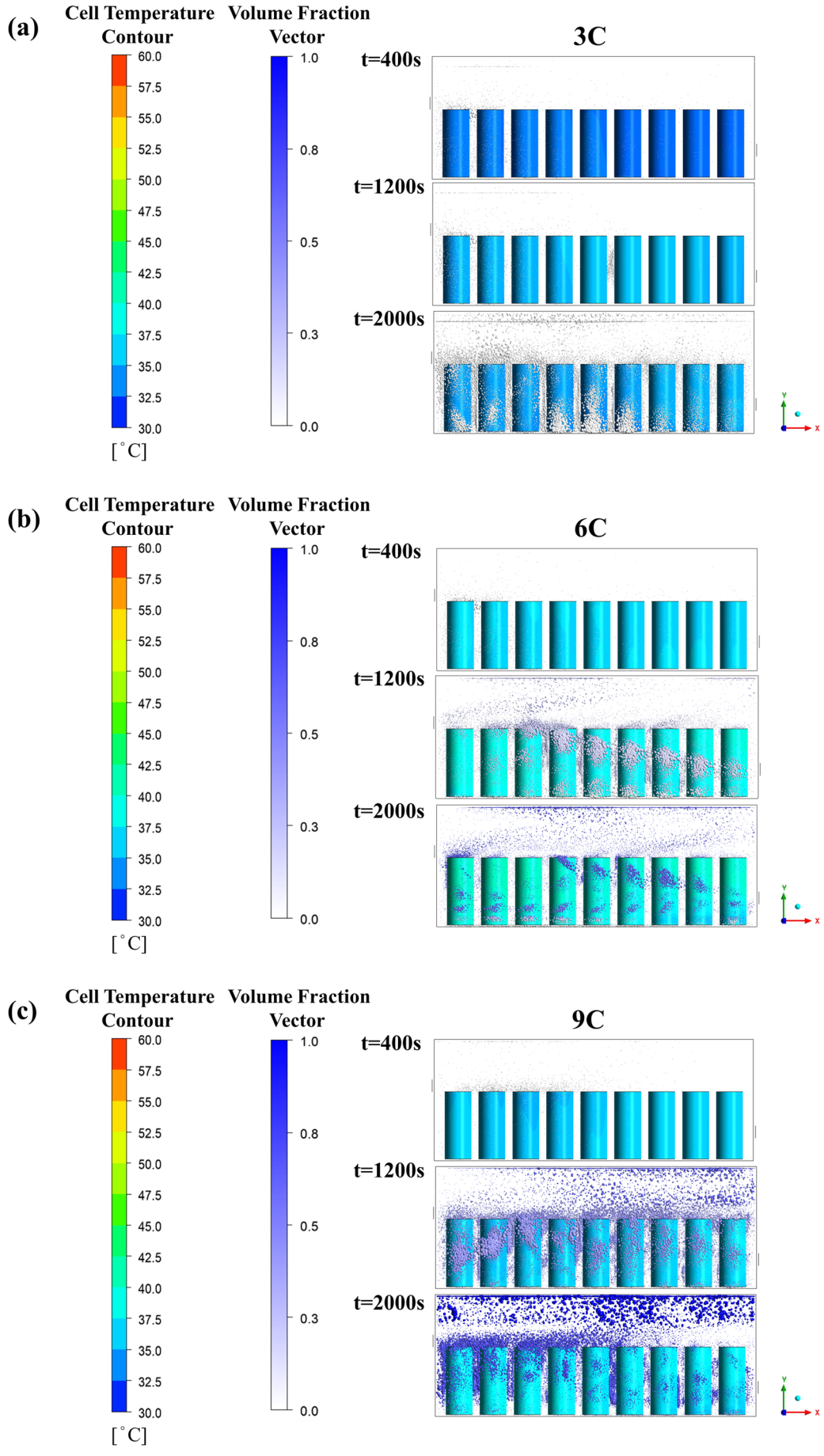


Figure 13. Gas-liquid phase distribution of Novec7000 module at different times under two-phase immersion cooling. (**a**) 3C, (**b**) 6C, (**c**) 9C.

6. Conclusions

In this study, a three-dimensional geometric model and a numerical simulation framework for two-phase immersion cooling of battery modules were established, incorporating LFP battery material properties, battery thermal generation conditions, coolant properties, and relevant boundary conditions. This study used the maximum temperature difference, vapor fraction, and temperature standard deviation as evaluation indicators to analyze the heat-transfer behavior and heat-dissipation performance of the two-phase immersion-cooled system under different operating conditions. FS49, SF33, Novec 7000, and R141b are considered as the coolants. To ensure the reliability of the simulation results, the model was first validated against experimental data on battery heat generation, and a mesh independence analysis was also performed to confirm the stability and accuracy of the results. Based on cross-comparison and quantitative analysis of the thermal and flow fields from variable simulations, the following conclusions can be drawn:

- Under 9C high-rate discharge, R141b, with its low boiling point, reaches nuclear boiling first, utilizing its latent heat of vaporization to stabilize the battery temperature rise within a gradual range. The highest module temperature of R141b is 14.81 °C lower than that of FS49, which maintains single-phase flow throughout (a reduction of approximately 25.4%). Its temperature control performance is significantly better than that of high-boiling-point coolants, maintaining single-phase flow, demonstrating the importance of the latent heat mechanism under extreme heat loads.
- Comprehensive analysis of all variables shows that the performance of two-phase immersion cooling is affected by the coupling of multiple physical quantities, including boiling point, latent heat, and heat generation rate. The optimal thermal management scheme should achieve a dynamic balance between reducing peak temperature and improving temperature uniformity. Especially for high-power applications, using physical phase-change mechanisms is far more engineering-efficient.
- A moderate heat load can stably trigger phase change and optimize the flow field and temperature uniformity, but under extremely high loads, excessively dense bubbles will hinder liquid phase return and lead to increased local temperature differences. Therefore, the design of a two-phase immersion cooling system must balance the benefits of latent heat of vaporization against the adverse effects of bubble accumulation on the flow field.
- SF33, Novec 7000, and R141b coolants have better temperature rise control at 3C discharge rate, with average temperatures of 35.17 °C, 36.03 °C, and 34.13 °C respectively, and their temperature standard deviations are all within 1.5 °C.

Author Contributions: W.-M.Y.: conceptualization, methodology, supervision; S.R.: data curation, writing—original draft preparation; W.-K.W.: visualization, investigation, software, validation; C.-H.L.: writing—reviewing and editing. All authors have read and agreed to the published version of the manuscript.

Funding: This research was funded by the National Science and Technology Council (NSTC 113-2221-E-027-118-MY2) in Taiwan.

Institutional Review Board Statement: Not applicable.

Informed Consent Statement: Not applicable.

Data Availability Statement: Not applicable.

Conflicts of Interest: The authors declare no conflict of interest.

Use of AI and AI-Assisted Technologies: During the preparation of this work, the authors used ChatGPT to improve the English phrasing and grammar. After using this tool, the authors reviewed and edited the content as needed and take full responsibility for the published article.

Nomenclature

Symbol	Definition
C_{evap}	Evaporation phase-change coefficient
C_{cond}	Condensation phase-change coefficient
C_P	Specific heat at constant pressure [J/kgK]
E_{oc}	Open-circuit voltage [V]
$\vec{F}$	Surface tension force [N/m^3]
h	Convective heat transfer coefficient [W/m^{2}K]
H_a	Height of battery module [m]
H_c	Battery height [m]
I	Current [A]
k	Thermal conductivity [W/Mk]
L_a	Length of battery module [m]
L_f	Latent heat of vaporization of coolant [J/kg]

$\dot{m}$	Phase-change mass transfer rate [kg/s]
$\dot{m}_{lv}$	Phase-change mass transfer rate (liquid to vapor) [kg/s]
$\dot{m}_{vl}$	Phase-change mass transfer rate (vapor to liquid) [kg/s]
N	Total number of batteries
P	Pressure [Pa]
P_1	Coolant inlet velocity monitoring point
P_2	Coolant outlet velocity monitoring point
P_3	Flow-field velocity monitoring point inside module
P_4	Temperature monitoring point (upper surface)
P_5	Temperature monitoring point (center)
$q'''_{battery}$	Volumetric heat generation rate of battery module [W/m^3]
S	Mass source term [kg/m^{3}s]
t	Time [s]
T	Temperature [K]
T_i	Average temperature of the ith battery [K]
U	Actual operating voltage [V]
$\vec{v}$	Velocity vector [m/s]
V	Volume [m^3]
V_f	Total volume of the fluid domain [m^3]
W_a	Width of battery module [m]
Greek Symbols	
ϕ_c	Battery diameter [m]
ϕ_i	Inlet diameter [m]
ϕ_o	Outlet diameter [m]
δ	Thickness of battery module [m]
Δ	Variation/Change
α	Volume fraction
ρ	Density [kg/m^3]
∂	Partial differential operator
∇	Nabla operator [m^{-1}]
μ	Kinematic viscosity [Pa.s]
σ	Surface tension coefficient [N/m]
κ	Interfacial curvature [m^{-1}]
Subscripts	
a	Battery module
avg	Average
b	Battery
l	Liquid
max	Maximum
min	Minimum
q	Fluid phase
sat	Saturation
T	Temperature
v	Vapor

References

1. Bai, P.; Xu, R.; Liu, M.; et al. Thermal Runaway Characteristics of LFP Batteries by Immersion Cooling. *ACS Appl. Energy Mater.* **2023**, *6*, 7205–7211. https://doi.org/10.1021/acsaem.3c00904.
2. Guo, L.S.; Wang, Z.R.; Wang, J.H.; et al. Effects of the environmental temperature and heat dissipation condition on the thermal runaway of lithium ion batteries during the charge-discharge process. *J. Loss Prev. Process Ind.* **2017**, *49*, 953–960. https://doi.org/10.1016/j.jlp.2017.05.029.
3. Yin, C.; Zhang, Y.; Sheng, L.; et al. Assessments of thermal-runaway behaviors in a NCM811-based cylindrical lithium-ion battery. *J. Power Sources* **2026**, *671*, 239555. https://doi.org/10.1016/j.jpowsour.2026.239555.
4. Gong, X.; Wong, S.K.; Ye, H.; et al. Traced state of charge for lithium-ion battery thermal runaway accidents. *J. Energy Storage* **2026**, *148*, 120133. https://doi.org/10.1016/j.est.2025.120133.
5. Yang, T.F.; Zheng, L.Z.; Lin, C.Y.; et al. A comprehensive parametric study on thermal aspects of vanadium redox flow batteries. *J. Therm. Anal. Calorim.* **2023**, *148*, 14081–14096.
6. Yang, T.F.; Zheng, L.Z.; Teng, L.T.; et al. Performance analysis of vanadium redox flow battery with interdigitated flow channel. *Therm. Sci. Eng. Prog.* **2024**, *47*, 102360. https://doi.org/10.1016/j.tsep.2023.102360.
7. Yao, J.; Zhang, T.; Han, Z.; et al. Study on the effect of immersion thermal management for high-current rate fast charging of 21700 Li-ion batteries. *J. Energy Storage* **2024**, *85*, 111061. https://doi.org/10.1016/j.est.2024.111061.
8. Xin, Z.; Tang, W.; Yao, W.; et al. A review of thermal management of batteries with a focus on immersion cooling. *Renew. Sustain. Energy Rev.* **2025**, *217*, 115751. https://doi.org/10.1016/j.rser.2025.115751.

9. Yang, T.F.; Lin, P.Y.; Lin, C.Y.; et al. Study on thermal aspects of lithium-ion battery packs with phase change material and air cooling system. *Case Stud. Therm. Eng.* **2024**, *53*, 103809. https://doi.org/10.1016/j.csite.2023.103809.
10. Qi, W.; Liu, Y.; Wang, X.; et al. Performance enhancement of battery thermal management based on liquid cooling plate channels embedded with non-uniform spiral fin structures. *Appl. Therm. Eng.* **2026**, *300*, 131501. https://doi.org/10.1016/j.applthermaleng.2026.131501.
11. Sheng, L.; Wang, H.; Zhang, C.; et al. Experimental study on immersion cooling performance of a lithium-ion battery module for commercial/industrial energy storage at different ambient temperatures. *Int. J. Therm. Sci.* **2026**, *221*, 110473. https://doi.org/10.1016/j.ijthermalsci.2025.110473.
12. Huang, H.; Li, W.; Xiong, S.; et al. Single-phase static immersion-cooled battery thermal management system with finned heat pipes. *Appl. Therm. Eng.* **2024**, *254*, 123931. https://doi.org/10.1016/j.applthermaleng.2024.123931.
13. Liu, Q.; Sun, C.; Zhang, J.; et al. The electro-thermal equalization behaviors of battery modules with immersion cooling. *Appl. Energy* **2023**, *351*, 121826. https://doi.org/10.1016/j.apenergy.2023.121826.
14. Chandrasekaran, M.; Jithin, K.V.; Soundarya, T.; et al. Comprehensive experimental study of battery thermal management using single-phase liquid immersion cooling. *J. Energy Storage* **2025**, *111*, 115445. https://doi.org/10.1016/j.est.2025.115445.
15. Wahab, A.; Cifterler, N.; Amjady, N.; et al. Enhancing energy and thermal efficiency of single-phase liquid immersion cooling systems for lithium-ion batteries in electric vehicles. *J. Energy Storage* **2025**, *131*, 117365. https://doi.org/10.1016/j.est.2025.117365.
16. Hu, J.; Yu, B.; Chen, Z.; et al. Simulation Study on the Single-Phase Immersion Cooling Performance of Lithium-Ion Battery Packs. *Appl. Sci.* **2025**, *15*, 9531. https://doi.org/10.3390/app15179531.
17. Choi, H.; Lee, H.; Kim, J.; et al. Hybrid single-phase immersion cooling structure for battery thermal management under fast-charging conditions. *Energy Convers. Manag.* **2023**, *287*, 117053. https://doi.org/10.1016/j.enconman.2023.117053.
18. Li, Y.; Bai, M.; Zhou, Z.; et al. Thermal management for the prismatic lithium-ion battery pack by immersion cooling with Fluorinated liquid. *Appl. Therm. Eng.* **2024**, *257*, 124453. https://doi.org/10.1016/j.applthermaleng.2024.124453.
19. Li, C.; Wang, Y.; Sun, Z.; et al. Two-phase immersion liquid cooling system for 4680 Li-ion battery thermal management. *J. Energy Storage* **2024**, *97*, 112952. https://doi.org/10.1016/j.est.2024.112952.
20. Liu, X.; Zhou, Z.; Wu, W.T.; et al. Numerical simulation for comparison of cold plate cooling and HFE-7000 immersion cooling in lithium-ion battery thermal management. *J. Energy Storage* **2024**, *101*, 113938. https://doi.org/10.1016/j.est.2024.113938.
21. Williams, N.P.; Trimble, D.; O'Shaughnessy, S.M. An experimental investigation of liquid immersion cooling of a four cell lithium-ion battery module. *J. Energy Storage* **2024**, *86*, 111289. https://doi.org/10.1016/j.est.2024.111289.
22. Zhou, H.; Dai, C.; Liu, Y.; et al. Experimental investigation of battery thermal management and safety with heat pipe and immersion phase change liquid. *J. Power Sources* **2020**, *473*, 228545. https://doi.org/10.1016/j.jpowsour.2020.228545.
23. Kureshi, D.A.; Nandan, R.; Das, M.K. Improved temperature uniformity and fast charging of high energy density Li-ion battery module via two-phase immersion cooling. *Appl. Therm. Eng.* **2026**, *290*, 130105. https://doi.org/10.1016/j.applthermaleng.2026.130105.
24. Bai, H.; Li, X.; Zhou, Z.; et al. Efficient thermal management of lithium-ion battery modules using a simplified two-phase immersion cooling system. *Appl. Therm. Eng.* **2026**, *290*, 129993. https://doi.org/10.1016/j.applthermaleng.2026.129993.
25. Banerjee, R.; Nidhul, K. Immersion cooling performance of nanofluid in a cylindrical cell battery pack using two-phase numerical simulations for varying discharge rates: A comparative study. *Results Eng.* **2025**, *25*, 104377. https://doi.org/10.1016/j.rineng.2025.104377.
26. Koucheh, A.B.; Sharbati, P.; Ünlü, C.; et al. Comprehensive evaluation of battery cooling mechanisms including two-phase immersion with 3M™ NOVEC™-7000 and 7100. *Energy Convers. Manag.* **2026**, *348*, 120780. https://doi.org/10.1016/j.enconman.2025.120780.
27. Lee, W.H. A Pressure Iteration Scheme for Two-Phase Flow Modeling. In *Multiphase Transport: Fundamentals, Reactor Safety, Applications*; Hemisphere Publishing Corp.: Washington, DC, USA, 1980; Volume 1, pp. 407–432.
28. Kharangate, C.R.; Mudawar, I. Review of computational studies on boiling and condensation. *Int. J. Heat Mass Transf.* **2017**, *108*, 1164–1196. https://doi.org/10.1016/j.ijheatmasstransfer.2016.12.065.
29. Alizadehdakhel, A.; Rahimi, M.; Alsairafi, A.A. CFD modeling of flow and heat transfer in a thermosyphon. *Int. Commun. Heat Mass Transf.* **2010**, *37*, 312–318. https://doi.org/10.1016/j.icheatmasstransfer.2009.09.002.
30. Zhou, L.; Yang, W.; Li, C.; et al. Numerical Investigation on Thermal Performance of Two-Phase Immersion Cooling Method for High-Power Electronics. *Front. Heat Mass Transf.* **2024**, *22*, 157–173. https://doi.org/10.32604/fhmt.2023.045135.
31. Jiang, W.; Lyu, P.; Liu, X.; et al. Temperature equalization strategy in immersion flow boiling battery thermal management: Optimization of flow regime in boiling heat transfer. *Appl. Therm. Eng.* **2025**, *267*, 125825. https://doi.org/10.1016/j.applthermaleng.2025.125825.
32. Jiang, W.; Lyu, P.; Liu, X.; et al. Evaluation of thermal performance of immersion flow boiling thermal management in large-scale battery packs with simplified model. *Int. Commun. Heat Mass Transf.* **2025**, *162*, 108656. https://doi.org/10.1016/j.icheatmasstransfer.2025.108656.

33. Bernardi, D.; Pawlikowski, E.; Newman, J. A General Energy Balance for Battery Systems. *J. Electrochem. Soc.* **1985**, *132*, 5–12. https://doi.org/10.1149/1.2113792.
34. Wang, Y.; Li, C.; Wen, X.; et al. Experimental studies on two-phase immersion liquid cooling for Li-ion battery thermal management. *J. Energy Storage* **2023**, *72*, 108748. https://doi.org/10.1016/j.est.2023.108748.
35. Li, Y.; Bai, M.; Zhou, Z.; et al. Experimental investigations of liquid immersion cooling for 18650 lithium-ion battery pack under fast charging conditions. *Appl. Therm. Eng.* **2023**, *227*, 120287. https://doi.org/10.1016/j.applthermaleng.2023.120287.
36. Williams, N.P.; Trimble, D.; O'Shaughnessy, S.M. Liquid immersion thermal management of lithium-ion batteries for electric vehicles: An experimental study. *J. Energy Storage* **2023**, *72*, 108636. https://doi.org/10.1016/j.est.2023.108636.
37. Williams, N.P.; Trimble, D.; O'Shaughnessy, S.M. Electrochemical-thermal numerical model of a lithium-ion battery under natural convection liquid immersion cooling conditions. *Energy Convers. Manag. X* **2025**, *27*, 101062. https://doi.org/10.1016/j.ecmx.2025.101062.